

# A Bio-Inspired Adjustable Posture Quadruped Robot with Laterally Undulating Spine for Terradynamically Challenging Environments

Saurav Kumar Dutta<sup>1</sup> and Yasemin Ozkan Aydin<sup>1</sup>

<sup>1</sup>Department of Electrical Engineering, University of Notre Dame, Notre Dame

April 12, 2024

## Abstract

Adaptation of morphology in response to varying environments is a crucial feature seen in biological organisms. While some robots emulate adaptability through the use of adaptive body parts, practical implementation of morphological transformations in robotics remains limited. This limitation arises due to the complexity of such transformations, demanding the fusion of advanced materials, control systems, and design approaches. In our paper, we introduce a bioinspired quadruped robot equipped with a laterally undulating spine, designed to adapt its posture specifically for navigating complex terradynamic environments. Leveraging a symmetrical parallelogram mechanism, this robot can alter both height and width, enabling traversal across varied surfaces, collision avoidance, passage through narrow channels, and obstacle negotiation. Additionally, our robot's innovative design strategically positions its center of gravity within its support triangle throughout the gait cycle using lateral undulation, eliminating the need for posture-stabilizing sensors or learning algorithms.

# A Bio-Inspired Adjustable Posture Quadruped Robot with Laterally Undulating Spine for Terradynamically Challenging Environments

Saurav Kumar Dutta, Yasemin Ozkan-Aydin\*

**Abstract**—Adaptation of morphology in response to varying environments is a crucial feature seen in biological organisms. While some robots emulate adaptability through the use of adaptive body parts, practical implementation of morphological transformations in robotics remains limited. This limitation arises due to the complexity of such transformations, demanding the fusion of advanced materials, control systems, and design approaches. In our paper, we introduce a bio-inspired quadruped robot equipped with a laterally undulating spine, designed to adapt its posture specifically for navigating complex terradynamic environments. Leveraging a symmetrical parallelogram mechanism, this robot can alter both height and width, enabling traversal across varied surfaces, collision avoidance, passage through narrow channels, and obstacle negotiation. Additionally, our robot’s innovative design strategically positions its center of gravity within its support triangle throughout the gait cycle using lateral undulation, eliminating the need for posture-stabilizing sensors or learning algorithms.

**Index Terms**—Variable morphology, posture adaptability, lateral undulation, variable body angle, lateral sequence gait, creeping gait, kinematic gait formula, Hildebrand gait analysis.

## I. INTRODUCTION

**B**iological creature’s capacity to adapt to a variety of environments is greatly facilitated by morphological changes that increase its robustness [1]–[3]. The creatures adopt many different kinds of morphological changes to adapt themselves to the changing environment [4]. Pigeons are known to use a strategy of folding their wings to navigate through obstacles [5]. Also, to fly more efficiently and conserve energy, bats, and birds constantly fold and unfold their wings [6]. In addition to avoiding obstacles, several species of creatures like caterpillars [7] and salamanders [8], coil their bodies like a wheel and roll to avoid the predators.

Reptiles like crocodiles and alligators showcase morphological adaptability during locomotion, altering their body posture (from sprawling to semi-erect or erect, Fig.1) based on the movement of the femur relative to the body. This flexibility enables them to navigate differing speeds and surface conditions during movement [9]–[11]. For instance, crocodiles adopt a sprawling posture when walking at slower speeds, while they switch to a semi-erect posture for faster movement on dry surfaces [12]. Other legged animals like humans, dogs, cats, and horses, to name a few have mostly erect postures whereas salamanders and geckos have a sprawling posture.

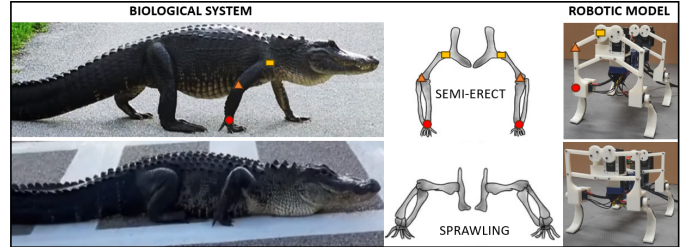


Fig. 1: Different postures seen in biological systems and our robotic model (top) Semi-erect posture in animal (left-middle) and our robotic model. Our robot model replicates the key joint locations of its animal counterparts: hip (yellow rectangles), knee (orange triangles), and ankle (red circles) joints. (bottom) Sprawling posture in animal (left-middle) and our robotic model (right). Animal images modified from publicly available websites.

Similar to biological systems, many researchers have developed robots with adaptive and re-configurable body parts to enhance their functionalities [13]–[25]. Moreover, adaptive behavior leads to the simplification of control [26] and robot design [27]. These robots with adaptive and re-configurable body parts can be broadly classified into three types. Some of these robots adapt their body shape to the environment they travel [13]–[19], while the others vary the type of wheel or limb they have [20]–[25] and some others undulate their spine or backbone laterally to enhance their locomotion and energy efficiency [28]–[31]. The mobile robot of Li et al. [13] has a transformable body that allows it to move both in open areas and narrow channels. Jiang et al. [14] use a balance-rocker mechanism that helps the robot change its posture and adapt to different terrain conditions. Similarly, the six-wheeled mobile robot of Song et al. [15] makes use of a Sarrus-variant mechanism to reconfigure the robot body for terrain adaptability and obstacle crossing. The robot in [17] reconfigures its shape for overcoming obstacles by using a four-bar extension mechanism. The robot of Derrouaoui et al. [18], which is an unmanned aerial system also makes use of rotating arms to increasingly become transformable as these arms enhance the maneuverability and agility of such systems. In [19], the robot uses an umbrella-inspired mechanism for changing its body shape. The robots that change their legs, Zheng et al. [20] use an adaptive wheel based on a gear mechanism for multi-terrain locomotion. An adaptive wheel is also used by Kim et al. [21] which uses a reconfigurable parallel mechanism to overcome stairways. The robot in [22] uses a directionally flexible, reconfigurable leg with a return spring to overcome obstacles. In [23], the robot’s body folds and unfolds itself to switch between wheel and claw mode. The amphibious robot [24] uses an adaptive propulsion mechanism wherein the mechanism switches

\*Corresponding author, email: yozkanay@nd.edu

Both authors are with the Department of Electrical Engineering, University of Notre Dame, Notre Dame, IN 46556 USA

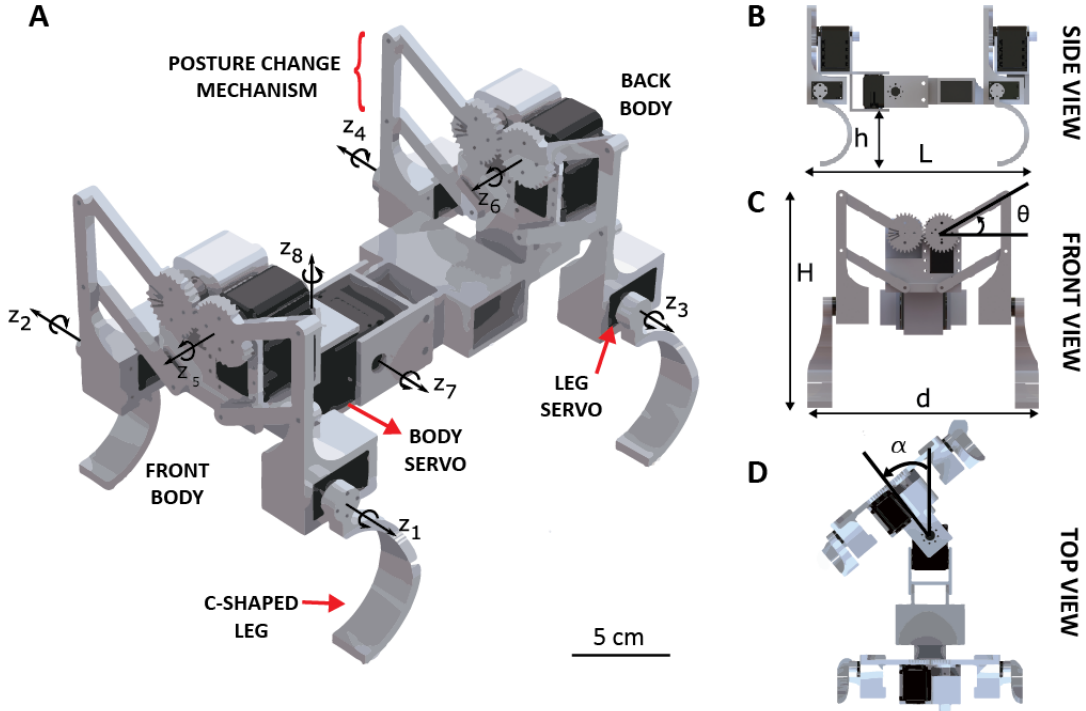


Fig. 2: Mechanical parameters of the robot. (A) An isometric view (perspective) of the 3-D CAD model showing the different parts along with the axes of rotation.  $z_1, z_2, z_3, z_4$  correspond to the axes of rotation of Dynamixel XL330-M288-T,  $z_5$  and  $z_6$  correspond to the axes of rotation of Dynamixel AX-12A,  $z_7$  and  $z_8$  correspond to the axes of rotation of Dynamixel 2XL430-W250-T. (B) Side view, L: Length, h: Distance from the ground to the base. (C) Front view, showing the posture change mechanism, d: Width, H: Height,  $\theta$ : Posture angle from the horizontal axis. (D) Top view, showing the lateral undulation,  $\alpha$ : Body angle.

between leg and flipper to move on the surface and underwater, respectively. Baines et al. [25] use a morphing limb in their bio-inspired amphibious robot. The morphing limb transitions between a flipper for swimming and a leg for walking. Apart from adaptive and re-configurable body parts, certain quadruped robots also employ a bio-inspired laterally undulating adaptive spine or backbone, which helps them not just in their locomotion [28]–[30] but also for energy-efficient climbing [31].

This paper presents the design and capabilities of a novel quadruped robot that leverages a bio-inspired, variable morphology. Our robot surpasses existing static-body designs [32]–[36] by transitioning between sprawled and semi-erect postures, enhancing maneuverability and obstacle traversal. Additionally, it incorporates lateral body undulation, further refining locomotion robustness, and gait stability.

The contribution of our paper can be summarized in three categories:

- i Posture changing mechanism - This paper presents a bioinspired, gear-driven, symmetrical parallelogram mechanism that enables a quadruped robot to replicate the posture adaptability of reptiles. Unlike conventional quadruped robots with fixed body shapes, this novel design allows the robot to not only alter its height but also adjust its body width through the side-to-side movement of the parallelogram links, mimicking the femur action in animals. This unique capability enhances the robot’s environmental adapt-

ability for traversing diverse terrain and obstacles.

- ii Simple design – We introduce a quadruped robot designed for efficient, sensorless navigation. Inspired by animal lateral gaits, the robot’s inherent stability stems from the careful center of gravity placement within the support polygon. This design choice avoids complex posture control systems, allowing the robot to traverse unstructured environments effortlessly. This simplicity and inherent stability translate to superior efficiency and robustness compared to sensor-dependent robots.
- iii Body undulation - The robot has been designed to walk with a peak amplitude of body angle,  $\alpha_{peak}$  of at least  $40^\circ$  and beyond. This particular feature helps the robot walk in various environment (especially climbing ramps) wherein the robot’s stability is enhanced by increasing  $\alpha_{peak}$ .

To the best of our knowledge, there is currently no known quadruped robot that integrates both a gear-driven symmetrical parallelogram mechanism for posture adjustment and body undulation, all designed based on bio-inspired principles of stability and gait selection. While few bio-inspired robots with variable posture exist (e.g., Bongard [1], Ansari et al. [37], Juárez-Campos et al. [38]), their approaches have limitations. Bongard’s robot [1] relies on a complex gear train and leg stands, limiting agility. Ansari et al.’s [37] utilize soft legs for posture, but possess a rigid spine, restricting gait versatility. Juárez-Campos et al.’s [38] Peaucellier-Lipkin mechanism offers

limited posture variations. Furthermore, extensive testing in unstructured environments for these robots is lacking, making performance comparisons difficult. The research presented in this paper represents a significant contribution to the field, as it highlights and substantiates, through experimental validation, the crucial role of morphology changes in bio-inspired quadruped robots when navigating challenging, unstructured environments. By allowing for posture and body angle adjustments across a wide range, these robots demonstrate a higher capacity to adapt to unfamiliar surroundings, making them particularly suitable for applications such as search and rescue operations during natural disasters.

The rest of the paper is organized as follows: Section II provides a summary of the components and procedures utilized to design, manufacture, and control the robot. Section III discusses stability and gait selection through bio-inspiration. Section ?? analyzes the footfall and gait of the robot. The experimental results are discussed in Section IV. Finally, Section V concludes the paper.

## II. MATERIALS and METHODS

### A. Robot Modeling and Design

The 3D computer-aided design (CAD) model of the robot is shown in Fig. 2. The robot has eight axes of rotation, which are denoted by  $z_{i,i=1,2,3,\dots,8}$  where  $z_1$ ,  $z_2$ ,  $z_3$ , and  $z_4$  correspond to the axes of rotation of the one degree of freedom (DoF) legs,  $z_5$  and  $z_6$  correspond to the axes of rotation of the two posture change mechanisms that are located at the front and back segments of the robot and  $z_7$  and  $z_8$  correspond to the pitch and yaw motions of the robot body, respectively.

1) Posture change mechanism: The posture change mechanism consists of two parallelogram mechanisms [39] which are synchronously operated by a single motor with the help of a gear drive (Fig. 2A). The opposite links in the parallelogram mechanism are of the same length. In the parallelogram, the length of the link with gear is the longest (60 mm). The length of the portion of the link between the two longest links is 44.5 mm, making the total length of this link 104.5 mm. For the gear drive, both the gears have a pitch circle diameter of 15 mm and a module (the ratio of the pitch diameter of the gear to its number of teeth) of 1 [40]. The range of the posture angle,  $\theta$  is between  $+40^\circ$  and  $-60^\circ$ . It may be noted that  $z_5$  and  $z_6$  correspond to a single degree of freedom as the two posture change mechanisms do not have motion relative to each other.

The most important design parameters of the robot are:  $d$  and  $H$ , as indicated in Fig. 2 C.  $d$  and  $H$  depend on the dimensions of the links in the parallelogram mechanism and the posture angle,  $\theta$ . Hence, the dimensions of the links in the parallelogram mechanism have been chosen in a way that  $d$  and  $H$  have a range of 52 mm and 60 mm, respectively, as indicated in Table I. The selected dimensions of the links in the posture change mechanism also ensure that  $\theta$  has a range of  $100^\circ$ . The dimensions

TABLE I: Design parameters of the robot (Refer Fig. 2)

Posture $\theta$	Width $d$	Height $H$	Length $L$	Ground clearance $h$
$40^\circ$	180	180	250	25
$0^\circ$	202	190	250	65
$-60^\circ$	150	240	250	110

of the links, including the range of posture change mechanisms for the smooth functioning of the robot without any interference between the links and the parts, have been selected by using GeoGebra and “animation, basic motion, and motion analysis” options in Solidworks 2022.

2) Body design: The robot’s body consists of two parts, front and back, interconnected by a 2-DoF body joint. The yaw movement of this joint aligns with the lateral undulation of the robot’s body. However, it is important to highlight that, in the context of this study, the robot’s body pitch motion is not utilized. The motor corresponding to the  $z_7$  axis is initialized at a zero-degree angle, as indicated in Fig. 2, and remains fixed at zero degrees throughout the robot’s operation.

The front body of the robot, from the  $z_8$  axis to the front face along the longitudinal axis, is 70mm long. Thus, the front body of the robot rotates by an angle  $\alpha$  with a radius of 70mm. The robot has been designed to walk with a peak amplitude of body angle,  $\alpha_{peak}$  of  $40^\circ$  and beyond. As the robot starts walking while laterally undulating its back, the body angle  $\alpha$  keeps oscillating between  $+\alpha_{peak}^\circ$  and  $-\alpha_{peak}^\circ$ . When the robot stops,  $\alpha$  comes back to  $0^\circ$ . If  $\alpha_{peak}$  is less than  $40^\circ$ , the robot becomes unstable and falls during walking. Increasing the  $\alpha_{peak}$  enhances the stability of the robot and is required especially when the robot climbs up and down the inclines.  $\alpha_{peak}$  for each of the 40, 0, and -60 degree postures of the robot without any interference between the limbs and the body are 70, 60, and 75 degrees, respectively.

While an external tethered power source is employed for powering the robot, we also integrated a battery box into the back segment of the robot, as illustrated in Figure 2, to facilitate future autonomous locomotion capabilities.

3) Legs: C-shaped legs have become a mainstay in RHex-type robots, showcasing exceptional performance on various terrains [35], [41]–[45]. The C-shaped legs provide a fair trade-off between the enhanced mobility of legged robots and the sturdy stability of wheels. This innovative design significantly boosted efficiency, speed, and overall mobility compared to earlier iterations such as compass and hinged four-bar legs [46]. The rolling contact point during stance effectively extends the leg’s effective length throughout the gait cycle and realizes the air and ground states with only one actuated degree of freedom (at the hip) [46], [47]. Importantly, C-shaped legs bypass the stalling situations that can plague small-wheeled robots encountering obstacles [35], [42].

Driven by the benefits of C-shaped legs outlined earlier, we used them in our robot design. The inner and outer diameters of the C-shaped legs are 30 mm and 35 mm, respectively. These legs make sure that  $h$  has a minimum

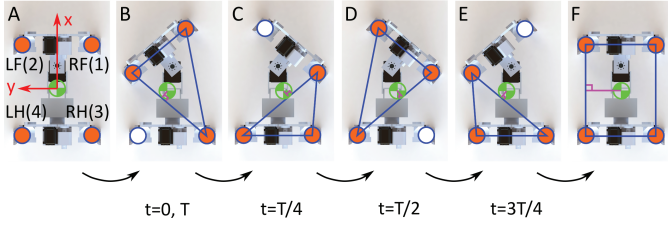


Fig. 3: Robot gait pattern: (A) The robot body rotates by an angle of  $+40^\circ$ . (B) (Beginning of the cycle) The left hind leg leaves the ground at  $t=0$  and completes one revolution in  $t=T/4$ . (C) The left fore leg leaves the ground at  $t=T/4$  to complete one revolution and at the same time, the body also undulates from its previous position to a current position of  $-80^\circ$  in  $t=T/2$ . (D) The right hind leg leaves the ground at  $t=T/2$  and completes one revolution in  $t=3T/4$ . (E) (End of the cycle) The right foreleg leaves the ground at  $t=3T/4$  to complete one revolution and at the same time, the body also undulates from its previous position to a current position of  $80^\circ$  in  $t=T$ . If the robot is run for more than 1 cycle, the steps keep repeating from (B) to (E). (F) The robot body rotates by an angle of  $-40^\circ$  to come back to its start position. In subfigures B-F the green circle shows the vertical projection of the robot's center of gravity (CoG) and the pink line shows the shortest path between the support triangle's edge and the CoG.

value of 25 mm at  $\theta = +40^\circ$  posture. This ensures ample space for maneuvering and obstacle avoidance, key to our robot's agility and performance.

## B. Prototype Development

After the design process and finalizing the model of the robot in Solidworks 2022, its parts are fabricated using a Stratasys F-170 3D printer with an Acrylonitrile Butadiene Styrene (ABS) plastic material. The final prototype of the robot is shown in Fig. 1. To increase the friction between the leg and the ground, the backside of all the legs is covered by a thin patch (3 mm) of rubber.

## C. Actuators and Electronics Integration

The robot uses a total of seven actuators, four Dynamixel XL330-M288-T (0.52 [N.m], 5V) motors for the legs, two Dynamixel AX-12A (1.5 [N.m], 11.1V) for the two posture change mechanisms and one Dynamixel 2XL430-W250-T (1.4 [N.m], 11.1V) for the lateral undulation. Each of the motors is independently controlled using Robotis U2D2 controller. U2D2 is assembled in the U2D2 Power Hub board, that is powered by a DC supply of 11 V. A voltage regulator is used to step down the supply of 11 V to the recommended voltage of 5 V for Dynamixel XL330-M288-T motors. The periodic motion of all the actuators is controlled by a program written in Matlab R2022b using the Robotis Dynamixel SDK Matlab library [48] and fed to the Robotis U2D2 controller.

There are pre-defined Dynamixel modes (position mode, velocity mode, etc.) [49] at which the Dynamixel servos can be operated. In this study, the legs are being operated using extended position control mode as this mode enables the leg servos to rotate beyond  $2\pi$  in either direction. This mode also enables the synchronous movement of the leg servos with the body servos. The posture change mechanisms are independent and do not have synchronous movement either with the leg or body servo. Hence, the

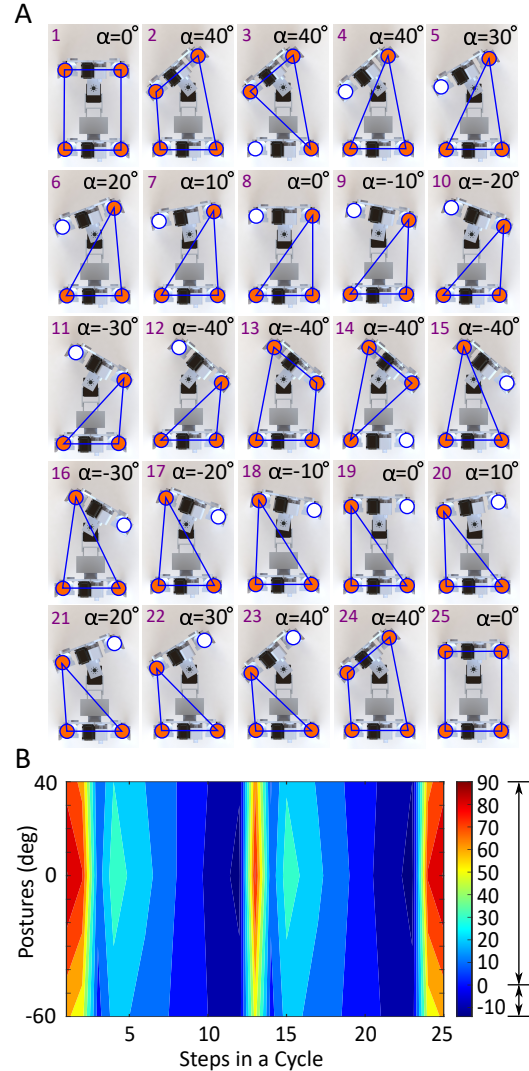


Fig. 4: Stability Map: (A) (1-25) Steps in the motion of the robot from the beginning to the end of one cycle. If the robot runs for multiple cycles, it starts from Step 1 and then keeps repeating the gait cycle between Steps 3 and 23. During the last step, it comes back to its initial position by following steps 24 and 25. Orange dots represent one of the binary states when the robot leg is on the ground, while the white dot represents the leg in the air. The blue polygon represents the support polygon or triangle. (B) The stability margin of the robot during the 25 steps of a cycle are plotted using contourf in Matlab for the three postures of the robot,  $-60^\circ$ ,  $0^\circ$  and  $40^\circ$ . The colorbar indicates the stability margin values. The robot is unstable (Us) when the stability margin is negative. The color represents the length of the shortest displacement vector (mm) from CoG to the support polygon, positive values mean the vector is inside the support polygon and the robot is stable. The above pictures of the robot with different configurations correspond to  $40^\circ$  posture. The pictures of the robot corresponding to  $-60^\circ$  and  $0^\circ$  postures are not shown here.

position control mode is used to control the servos of the posture change mechanism. The gait control of the robot is open-loop, i.e. the robot does not use any sensors and feedback, neither for posture stabilization nor for obstacle detection. The only feedback is from the servos of the robot for the closed-loop control of their angular displacements.

## III. STABILITY and GAIT SELECTION

To maintain static stability throughout the robot's walking motion, it is essential to ensure that the vertical

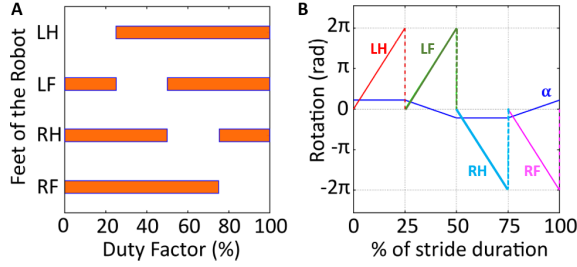


Fig. 5: Gait parameters: (A) Gait diagram. LH: Left hind foot. LF: Left forefoot. RH: Right hind foot. RF: Right forefoot. The orange bar denotes the percent of stride interval that each foot is on the ground (B) The sequence of motion of the legs and the back.  $\alpha$ : Body angle.

projection of the robot’s center of gravity consistently remains within the support pattern (a polygon formed by connecting the leg contact points of the robot [50]).

In the context of gait patterns, a lateral sequence gait is characterized by the hind foot of a quadruped making initial ground contact, followed by the forefoot on the same side of the body, according to Hildebrand [51]. Meanwhile, a creeping gait implies that a minimum of three feet maintain contact with the ground consistently [50].

In this paper, we adopted the lateral sequence creeping gait (Fig. 3). This choice stems from the fact that a creeping gait, as described in [52], guarantees a positive static stability margin across most of the gait cycle [50]. Furthermore, we selected the lateral sequence gait [51] in light of its advantages: (1) the area enclosed by the support triangle is greater than that enclosed by the support triangle for a diagonal sequence gait [53] and (2) a lateral sequence gait helps in the lateral undulation of a quadruped [54].

McGhee and Frank [50] define stability margin as the shortest path between any location on the support triangle’s edge and the center of gravity’s vertical projection. By drawing a normal from the center of gravity to the closest edge of the support triangle and measuring the normal, one can determine the stability margin, as shown in Fig. 3 where the length of the pink-colored normals indicates the stability margins of the robot. As long as the stability margins are greater than zero, the robot is statically stable. By following the above procedure, the robot’s motion cycle is divided into equally spaced 25 steps (Fig. 4), with each step showing a particular configuration and leg contact points of the robot. Then, the stability margins of the robot for these 25 steps for three postures of the robot,  $-60^\circ$ ,  $0^\circ$ , and  $40^\circ$  are obtained using Solidworks. These values are then utilized to generate the contour plot shown in Fig. 4. For all the postures, the stability margins are the greatest for steps 1, 2, 13, 24, and 25, when the four legs touch the ground. The stability margins are positive for all the steps except for steps 10, 11, 12, 21, 22, and 23. During these steps, the foreleg remains in the air and the robot tends to fall in the forward direction. However, before the robot body could fall and touch the ground, the foreleg completes its rotation and touches the ground first, and the robot regains its stability. From Fig. 4, it can be seen that in the immediate step after steps 12 and

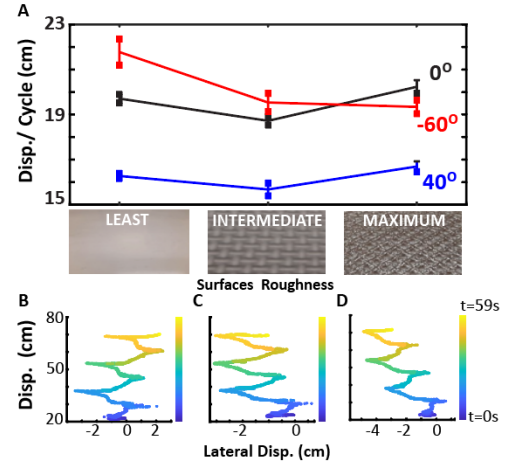


Fig. 6: Walking parameters of the robot: (A) Mean  $\pm$  SD of the CoM displacement per cycle for different postures ( $-60^\circ$ ,  $0^\circ$ ,  $40^\circ$ ) on surfaces of three different roughnesses (five trials and three cycles per trial). Example CoM displacement of the robot with  $40^\circ$  posture for three cycles when it walks on the surface with (B) least, (C) intermediate, and, (D) maximum roughness. The color bar indicates the time.

23, the four legs maintain contact with the ground and the stability margin becomes greatly positive from negative.

To maintain a lateral sequence creeping gait throughout the robot’s walking motion, it is essential to ensure that its three legs remain in contact with the ground during each instant of a cycle. For optimal locomotion efficiency, it is preferable that all four legs do not remain in contact with the ground simultaneously at any point during a cycle. Both these conditions are possible only when the footfalls of all four feet of the robot are evenly spaced in time. The gait diagram [55] and the sequence of motion of the legs and the body angle for the lateral sequence creeping gait are shown in Fig. 5. From Figs. 3 and 5, it can be seen that each of the legs remains in the air for the same amount of time (25%) during a cycle while the other three legs are in contact with the ground. Hence, according to Hildebrand’s gait formula, the robot has a gait formula of (75,25) [51]. Here, the first variable corresponds to the percentage of time that each hindfoot is on the ground during a cycle or stride (duty cycle) and the second variable corresponds to the percentage of time when a forefoot falls on the ground behind a hindfoot on the same side of the body during a stride (relative phase) [51], [56]. McGhee [56] generalizes Hildebrand’s gait formula to include the duty factor of each of the legs of a quadruped and the relative phases of any three legs, concerning a chosen fourth leg. According to McGhee’s gait formula [56],  $\mathbf{g}$  the robot’s gait is given as

$$\mathbf{g} = (0.75, 0.75, 0.75, 0.75, 0.5, 0.75, 0.25)^T. \quad (1)$$

In Eq.1, the first four variables correspond to the duty factors of the first, second, third, and fourth legs. The remaining three variables correspond to the relative phases of the second, third, and fourth legs concerning the first leg. In addition to the gait diagram (Fig. 5), this gait formula can also be calculated or obtained from the robot’s gait matrix,  $\mathbf{G}$ , and the duration vector,  $\mathbf{t}$  [56]. For writing  $\mathbf{G}$  and  $\mathbf{t}$ , the legs have been numbered as shown in Fig. 3.

The matrix  $\mathbf{G}$  comprises four columns, representing the four legs of the robot, while the total number of rows is equal to the length of one cycle of the gait sequence [56].

$$\mathbf{G} = \begin{bmatrix} 0 & 0 & 0 & 0 \\ 0 & 0 & 0 & 1 \\ 0 & 0 & 0 & 0 \\ 0 & 1 & 0 & 0 \\ 0 & 0 & 0 & 0 \\ 0 & 0 & 1 & 0 \\ 0 & 0 & 0 & 0 \\ 1 & 0 & 0 & 0 \end{bmatrix}, \mathbf{t} = \begin{bmatrix} 0 \\ T/4 \\ 0 \\ T/4 \\ 0 \\ T/4 \\ 0 \\ T/4 \end{bmatrix} \quad (2)$$

In Eq. 2,  $T$  is the stride duration, and the values within  $\mathbf{G}$  are binary, with 0 indicating a leg in contact with the ground and 1 indicating a leg lifted into the air [56]. The gait formula in Eq. 1 gives information only about the duty factor and relative phases of the legs. A quadruped robot's supporting feet position concerning its vertical center of gravity projection, along with its duty factor and relative phases, are all completely specified by a kinematic gait formula [50]. The kinematic gait formulae of the robot for  $\theta = 40^\circ$ ,  $0^\circ$  and,  $-60^\circ$  with  $\alpha_{peak} = 0^\circ$  for each of them are given as

$$\begin{aligned} k_{40^\circ} &= (0.75, 0.75, 0.75, 0.75, 0.681, 0.681, -0.509, \\ &\quad -0.509, 0.479, -0.472, 0.479, -0.472, 0.5, 0.75, 0.25)^T \\ k_{0^\circ} &= (0.75, 0.75, 0.75, 0.75, 0.564, 0.564, -0.421, -0.421, \\ &\quad 0.467, -0.467, 0.467, -0.467, 0.5, 0.75, 0.25)^T \\ k_{-60^\circ} &= (0.75, 0.75, 0.75, 0.75, 0.509, 0.509, -0.381, \\ &\quad -0.381, 0.289, -0.284, 0.289, -0.284, 0.5, 0.75, 0.25)^T \end{aligned} \quad (3)$$

In Eq.3, the first four and the last three variables denote the duty factors and the relative phases of the legs, respectively. The fifth, sixth, seventh, and eighth variables correspond to the x-coordinate, and the ninth, tenth, eleventh, and twelfth variables correspond to the y-coordinate of the dimensionless initial foot position of the legs of the robot. The origin lies at the center of the gravity of the robot with the x-axis pointing towards the direction of motion of the robot, and the y-axis pointing ninety degrees to the left of the x-axis (Fig. 3). The scale of the x and y coordinate axes is chosen such that stride length is equal to 1 [50].

Note that in Eq. 3, the first four and the last three variables are the same in magnitude as the robot has the same gait for all of its postures. The fifth, sixth, seventh, eighth, ninth, tenth, eleventh, and twelfth variables have different magnitudes for different postures of the robot. This is because with posture change, the initial dimensionless foot positions of the robot to its center of gravity change. Also, the stride length (distance covered by the robot in one cycle) changes with posture change. Therefore, the kinematic gait formula turns out to be different for different postures of the robot despite adopting the same gait. The kinematic gait formula is much more informative as it gives information about the duty factor, relative

phase, initial foot positions, center of gravity, and stride length. We used the motion analysis option in Solidworks to determine the initial foot positions, center of gravity, and stride length for obtaining the kinematic gait formulae (Eq. 3) for the three postures of the robot.

#### IV. EXPERIMENTAL RESULTS

The robot's performance in terms of overcoming hurdles without falling (robot body striking the ground) in different unstructured environments is carried out with a gait formula of (75,25) and peak amplitude of body angle,  $\alpha_{peak}$  of  $40^\circ$  except for the ramp experiments.

##### A. Flat surface

The robot's locomotion was assessed across diverse postures during three walking cycles on distinct flat surfaces, each featuring varying levels of roughness (Fig. 6). These surfaces encompass a whiteboard, characterized by minimal roughness, a foam mat with intermediate roughness, and a spiked plastic plate presenting the highest degree of roughness. Surface roughness levels were ascertained through visual inspection.

The robot's center of mass (CoM) motion was captured using the OptiTrack Motion Capture System for three specific postures:  $40^\circ$ ,  $0^\circ$ , and  $-60^\circ$  on each of the three surfaces. These three postures are chosen because as mentioned in Section II, the posture angle,  $\theta$  has minimum and maximum values of  $-60^\circ$  and  $40^\circ$ , respectively. The robot can attain any posture between these two values. For analysis, an intermediate posture of  $0^\circ$  is also chosen. The motion of the robot was recorded for five trials starting from the same initial position. The mean and standard deviation (SD) values of the captured motion are shown in Fig. 6 A. For  $-60^\circ$  posture, the displacement per cycle of the robot, as shown in Fig. 6 A is highest when it moves on the surface with the least roughness, followed by the surfaces with intermediate and maximum roughness. This is because, during the robot's locomotion, the hind legs mostly slide forward (SI movie- 0:33 to 0:44). This sliding is smooth and fast if the surface is smooth. As the surface gets rough, the hind legs tend to get stuck in the mechanical asperities as they move forward and hence the sliding is not smooth and fast. Similar to  $-60^\circ$  posture, the displacement per cycle follows a pattern for  $40^\circ$  and  $0^\circ$  postures, when the robot moves on surfaces with least and intermediate roughness, as shown in Fig. 6 A. However, contrary to  $-60^\circ$  posture, the robot's displacement per cycle for the  $40^\circ$  and  $0^\circ$  postures becomes the greatest when it moves on the surface with maximum roughness. This is because during the locomotion, when the hind legs get stuck, the robot body tends to fall forward and the suspended foreleg touches the ground before it can complete the full  $2\pi$  revolution (SI movie- 0:08 to 0:32). When this happens, the robot covers a greater distance in a single cycle.

Ideally, the displacement per cycle of the robot, irrespective of the surface it walks on, should have been the

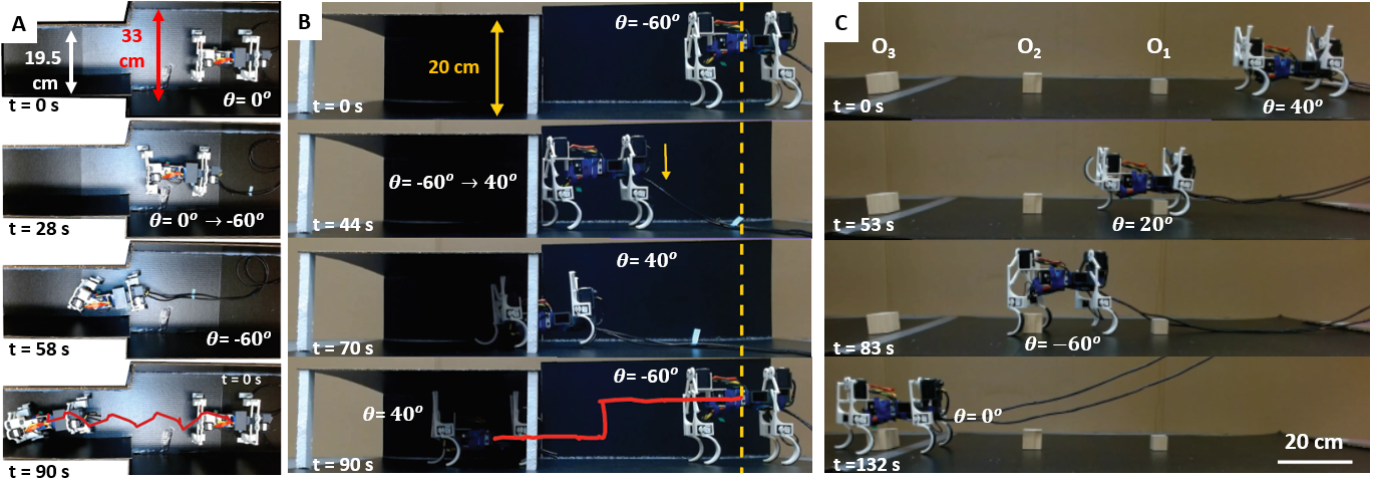


Fig. 7: (A) Moving from a wider (width= 330 mm) to a narrower channel (width= 195 mm) through posture change: At  $t = 0$  s with  $0^\circ$  posture. Posture change at  $t = 28$  s from  $0^\circ$  to  $-60^\circ$ . At  $t = 58$  s moves with  $-60^\circ$  posture. Trajectory tracking of the center of the robot from  $t=0$  s to  $t=90$  s. (B) Robot moving from an open area to a tunnel (height= 20 cm) through posture change. At  $t = 0$  s until  $t = 44$  s, it walks with  $-60^\circ$  posture. At  $t = 44$  s, it changes the posture from  $-60^\circ$  to  $40^\circ$ . At  $t = 70$  s and  $t = 90$  s, it walks with  $40^\circ$  posture. The red trajectory shows the movement of the center of the robot from  $t = 0$  s to  $t = 90$  s. (C) Moving over the different size of obstacles through posture change: At  $t = 0$  s with  $40^\circ$  posture, at  $t = 53$  s it passes the first obstacle ( $O_1 = 38 \times 38 \times 38 \text{ mm}^3$ ) with  $20^\circ$  posture, at  $t = 83$  s it passes the second obstacle ( $O_2 = 50 \times 50 \times 50 \text{ mm}^3$ ) with  $-60^\circ$  posture, and at  $t = 132$  s it passes the third obstacle ( $O_3 = 100 \times 50 \times 50 \text{ mm}^3$ ) with  $0^\circ$  posture.

highest for  $0^\circ$  posture followed by  $40^\circ$  and  $-60^\circ$  postures. This is because, at  $0^\circ$  posture,  $d$  (Table I) is highest, and the arc length subtended by the front body of the robot during lateral undulation is greatest and it covers a greater distance. At  $-60^\circ$  posture,  $d$  (Table I) is least and hence the arc length subtended by the body servo is less.

WE observed three cases when the hindlegs of the robot tend to get stuck. In the first case, the hind leg pasts that asperity after getting stuck initially, however, this leads to reduced displacement per cycle. In the second case, the robot tends to fall forward and the foreleg touches the ground before it completes a full  $2\pi$  revolution. In the third case, the robot deviates from its straight line path, and its trajectory bends, which results in the robot's lateral displacement, leading to a reduction in displacement per cycle of the robot, as shown in Figs. 6 B, C, and D. The robot's locomotion may fall under any of these three cases and hence the displacement per cycle can vary.

## B. Narrow Tunnel Traversal

Several trials were conducted to assess the robot's ability to navigate through different widths of channels (Fig. 7A) without and with adjusting its posture. As shown in Table I, the robot's width is at its maximum ( $d = 202$  mm) when the posture is set to  $0^\circ$ . Conversely, at a posture of  $-60^\circ$ , the robot's width is at its minimum ( $d = 150$  mm). The robot attempted to enter the narrower channel (width = 195 mm) after walking in a wider channel (width = 330 mm) with a fixed posture of  $0^\circ$ . However, this experiment was unsuccessful, as the robot collided with the side walls upon entering the narrower channel (SI movie- 1:06 to 1:16). Following the collision, the robot either remained stationary, attempting to enter the narrow channel or lost its stability and fell. Alternatively, the robot was tested by initially moving through a broader channel with a fixed posture of  $0^\circ$ , and upon reaching

the entry point of the narrower channel after completing one full cycle, the robot adjusted its posture from  $0^\circ$  to  $-60^\circ$ . Subsequently, the robot moved inside the narrower channel at a posture of  $-60^\circ$  (SI movie- 0:48 to 1:05). This sequence of actions was replicated five times, and in each repetition, the experiment resulted in a consistently successful outcome. Note that the robot does not have any obstacle-detecting sensor. Hence, while carrying out the experiments, the robot is placed at a pre-defined distance before the obstacle and the robot program is written in a way that the robot changes its posture after completing the pre-defined distance.

## C. Low-Clearance Avoidance

Similar to the last experiment where the robot moved through a narrow channel, in this experiment, the robot goes through a tunnel of low height (200 mm) by avoiding collision with the roof of the tunnel. As can be seen in Table I, the maximum height of the robot is 240 mm and it attains this height when it has a posture of  $-60^\circ$ . At  $40^\circ$  posture, the robot's height is least at 180 mm. The robot walks at  $-60^\circ$  posture before entering the tunnel. In the experiments, the robot with  $-60^\circ$  posture completes two cycles and stops at the entry point of the tunnel, as shown in Fig. 7B. At the entry point of the tunnel, the robot changes its posture from  $-60^\circ$  to  $40^\circ$ , which reduces the robot's height from 240 mm to 180 mm. Then, the robot at  $40^\circ$  posture moves inside the tunnel fully by completing two cycles (SI movie- 1:17 to 1:35). Without the posture change, the robot collides with the tunnel, loses its stability, and falls (SI movie- 1:36 to 1:45). This experiment also highlights the importance of posture change in averting head-on collisions.

## D. Obstacle Avoidance

This experiment shows how changing the robot's posture can be an effective way to overcome obstacles of

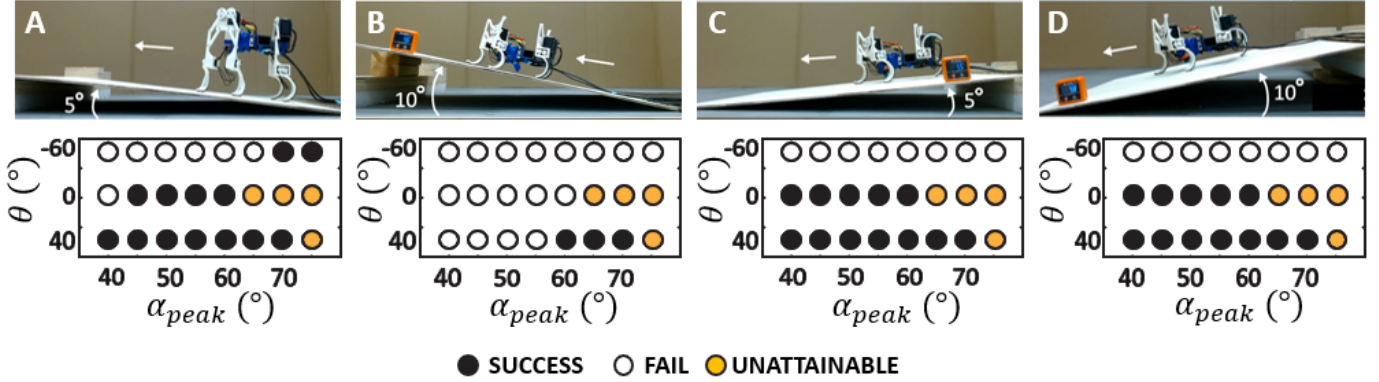


Fig. 8: Walking on a ramp (uphill/downhill) with different postures. The top row shows the example snapshots from the successful walking experiments. (A) 5° uphill with  $\theta = -60^\circ$  posture and  $\alpha_{peak} = 70^\circ$  body angle. (B) (10° inclination uphill) with 40° posture and 60° body angle. (C) (5° inclination downhill) with 40° posture and 40° body angle. (D) (10° inclination downhill) with 40° posture and 40° body angle. The bottom row shows the results of all the uphill/downhill experiments for the given surface angles (A. 5° uphill, B. 10° uphill, and C. 5° downhill, D. 10° downhill). The arrows show the direction of motion of the robot.

different sizes. By adjusting its posture, the robot can adapt to the shape and size of the obstacle on its path. It might not always be possible to circumvent obstacles, especially when the robot passes through a narrow tunnel with not enough space for the robot to go around. With posture change, the robot passes the obstacle without changing its path.

In these experiments, the robot traverses a level ground surface encountering three randomly sized obstacles, as shown in Fig. 7C. The first obstacle is a cube with an edge length of 38 mm. The second obstacle is also a cube with an edge length of 50 mm and is placed at a distance of 300 mm from the first obstacle. The third obstacle is a cuboid with a length of 100 mm, width and height each of 50 mm. It is placed at a distance of 350 mm from the second obstacle. The robot is placed at a distance of 200 mm ahead of the first obstacle. Due to the absence of obstacle-detecting sensors in the current version of the robot, the relative distance between the obstacles is manually selected such that the robot after completing a cycle is ahead of an obstacle and initiates a posture change.

At the beginning of the experiment, the robot is at 40° posture ( $h = 25$  mm, Table I). So, after completing one cycle, the robot stops in front of the second obstacle and changes its posture to 20° ( $h = 40$  mm). The robot at 20° posture overcomes the first obstacle in two cycles and stops at the second obstacle. It changes its posture to -40° at which  $h = 95$  mm. The robot at -40° posture overcomes the second obstacle in two cycles and stops at the third obstacle. It changes its posture to 0° at which  $h = 65$  mm. To overcome the third obstacle, the robot could have moved with -40° posture but at -40° posture, the distance between the legs is 140 mm. To increase the distance between the legs, the robot's posture is changed to 0° in which the distance between the legs is 162 mm. The robot at 0° posture overcomes the third obstacle by completing two cycles (SI movie- 1:46 to 2:17). Note that, the motion of the robot is open-loop, i.e. it was pre-programmed to change its postures after a fixed number of cycles. This experiment is carried out five times with a

TABLE II: Minimum and maximum displacement (Mean $\pm$ SD) of the robot for both uphill and downhill movement on a ramp for different postures ( $\theta$ ) and peak amplitude of body angles ( $\alpha_{peak}$ )

Ramp Type	$\theta$ (in degrees)	Mean $\pm$ SD (in cm)	$\alpha_{peak}$ (in degrees)
5° (uphill)	-60	14.1 $\pm$ 0.6	70
	0	Min: 13.7 $\pm$ 0.2 Max: 17.2 $\pm$ 0.4	45 60
	40	Min: 11.6 $\pm$ 0.1 Max: 17.1 $\pm$ 0.3	40 70
10° (uphill)	40	Min: 11.9 $\pm$ 0.4 Max: 12.9 $\pm$ 0.3	60 70
5° (downhill)	0	Min: 23.8 $\pm$ 0.2 Max: 24.9 $\pm$ 0.2	40 60
	40	Min: 19.7 $\pm$ 0.3 Max: 23.4 $\pm$ 0.1	45 70
10° (downhill)	0	Min: 27.5 $\pm$ 0.4 Max: 29 $\pm$ 0.2	40 60
	40	Min: 24.3 $\pm$ 0.4 Max: 28.5 $\pm$ 0.9	40 70

successful outcome each time.

To demonstrate the necessity of posture changes for the robot to successfully navigate the obstacles, a supplementary set of experiments is conducted. At 40° posture, the robot body strikes the first obstacle. After that, upon encountering the obstacle, the robot's body remains stationary in its current position, either attempting to move forward or becoming immobilized with its legs suspended in the air, without establishing contact with the ground surface (SI movie- 2:18 to 2:32). In another experiment, the robot overcomes the first obstacle at 20° posture and then tries to overcome the second obstacle without changing its posture. Similar to the prior case, following the robot body's collision with the second obstacle, it exhibits a behavior wherein the body remains stationary in an attempt to proceed, or it becomes immobilized atop the obstacle, with its legs suspended in the air and no

ground contact established.

Hence, the posture change mechanism enables the robot body to modify its height from the ground and the distance between its legs in response to obstructions in its path. This ability to modulate posture facilitates enhanced adaptability and maneuverability when navigating through complex environments and contributes to the robot’s agility and efficiency in negotiating obstacles effectively, thereby expanding its range of potential applications across diverse terrains and scenarios.

### E. Ramp Traversal

In this experiment, the robot’s stability is analyzed when it walks, both uphill and downhill, on  $5^\circ$  and  $10^\circ$  ramps. This experiment was considered important as in the previous subsections, the robot mostly moved on a flat surface while circumventing tunnels and obstacles through posture change. However, in real-world surroundings, the robot may need to walk through inclines and steep terrains with tunnels and rocks.

1) Uphill: The robot walks for four cycles on a  $5^\circ$  ramp with posture angle,  $\theta = 40^\circ$  and a peak amplitude of body angle,  $\alpha_{peak} = 40^\circ$  without falling. However, with  $0^\circ$  posture and  $40^\circ$  peak amplitude, the robot can complete two full cycles and falls at the start of the third cycle (SI movie- 3:30 to 3:39). For  $-60^\circ$  posture and  $40^\circ$  peak amplitude, the robot is unable to complete even one cycle and falls before that. Each of these experiments was carried out at least five times and similar observations were made each time.

To make the robot move for full four cycles with  $0^\circ$  and  $-60^\circ$  postures on a  $5^\circ$  ramp,  $\alpha_{peak}$  of the robot is increased to  $45^\circ$ . With  $45^\circ$  peak amplitude, the robot completes full four cycles on a  $5^\circ$  ramp both with  $0^\circ$  (SI movie- 3:39 to 3:54) and  $40^\circ$  postures. However, with  $\alpha_{peak} = 45^\circ$  and  $\theta = -60^\circ$ , the robot is unable to complete even one cycle and falls. In order to make the robot move on a  $5^\circ$  ramp with  $\theta = -60^\circ$ ,  $\alpha_{peak}$  is sequentially increased from  $45^\circ$  to  $75^\circ$  with an increment of  $5^\circ$ . The robot at  $\theta = -60^\circ$  kept falling in the first cycle itself for different values of  $\alpha_{peak}$  except when  $\alpha_{peak} = 70^\circ$ . With  $\theta = -60^\circ$  and  $\alpha_{peak} = 70^\circ$ , the robot could walk for a full four cycles on the  $5^\circ$  ramp without falling (SI movie- 2:33 to 2:47).

Next, the robot walks on a  $10^\circ$  ramp for four cycles. With  $\theta = 40^\circ$  and  $\alpha_{peak} = 40^\circ$ , the robot is unable to climb and falls without completing a single cycle. Hence,  $\alpha_{peak}$  is increased with an increment of  $5^\circ$ . With  $\theta = 40^\circ$  and  $\alpha_{peak} = 60^\circ$ , the robot can climb on a  $10^\circ$  ramp for four cycles (SI movie- 2:48 to 3:01). However, with  $\theta = 0^\circ$  and  $\alpha_{peak} = 60^\circ$ , the robot can complete only one cycle and falls in the second cycle. With  $-60^\circ$  posture, the robot is not able to complete even one cycle and falls irrespective of the  $\alpha_{peak}$  value.

Note that when the robot undergoes a posture change, it becomes notably less stable, a phenomenon that becomes especially pronounced when navigating inclines as opposed to flat terrain. Therefore, the experiments conducted

above demonstrate that, during incline traversal, enhancing the peak amplitude of the body angle across all body postures can significantly improve the robot’s stability. The performance of the robot in terms of its ability to complete full four cycles during uphill movement for different postures and peak amplitude of body angles is shown in Fig.8 A and B. In Fig.8, “success” denotes the robot’s ability to complete all four cycles, while “Fail” indicates a scenario in which the robot’s legs do not interfere with other body parts, however, it is unable to complete all four cycles and falls before that. “Unattainable” refers to the configuration of the robot where the robot legs start interfering with other legs or the robot body and the motion gets locked. It may be noted that with  $\theta = 40^\circ$ , the robot can have a maximum peak amplitude of  $70^\circ$ . Similarly, the maximum peak amplitude for  $\theta = 0^\circ$  and  $\theta = -60^\circ$  is  $60^\circ$  and  $75^\circ$ , respectively. If  $\alpha$  gets bigger than its maximum peak amplitude, the robot reaches an unattainable or singular configuration. These experiments also show that during uphill movement, the stability of the robot also depends on the height of the robot body from the ground,  $h$  (Fig. 2). The lower the value of  $h$ , the greater the stability of the robot.

2) Downhill: The robot walks on a  $5^\circ$  ramp for three cycles. For  $40^\circ$  and  $0^\circ$  postures, the robot completes 3 cycles without falling for all the peak amplitudes, as shown in Fig. 8 C and D. The locomotion of the robot with  $40^\circ$  posture and  $40^\circ$  peak amplitude of body angle can be found in the SI movie- 3:01 to 3:16). As the robot moves down the ramp, it tends to fall towards the front irrespective of the posture and the body angle. This phenomenon gets more pronounced as the robot body’s height increases from the ramp surface. Thus, for  $-60^\circ$  posture, the robot falls on its front by tipping over rather than falling on the back side which is observed when the robot climbs up the ramp (SI movie- 3:55 to 4:01). With  $-60^\circ$  posture, the robot fails to complete one cycle and falls irrespective of the body angle. However, with  $-40^\circ$  posture, the robot climbs down the ramp for all the peak amplitudes. The locomotion of the robot with  $0^\circ$  posture and  $45^\circ$  peak amplitude can be found in the SI movie- 4:02 to 4:11.

Next, the robot walks on a  $10^\circ$  ramp for three cycles. Similar to the previous case, the robot completes 3 cycles without falling for all the body angles for  $40^\circ$  and  $0^\circ$  postures. For  $-60^\circ$  posture, the robot falls on its front by tipping over and is unable to complete one cycle. However, the robot can complete three cycles with  $-20^\circ$  postures for all the peak amplitude of body angles. The locomotion of the robot with  $40^\circ$  posture and  $40^\circ$  peak amplitude can be found in the SI movie- 3:17 to 3:27. Table III shows the different postures to be used by the robot for moving in different types of unstructured environments.

### F. Outdoor experiments

The adaptable nature of the robot body also helps it to overcome and circumvent obstacles in outdoor settings

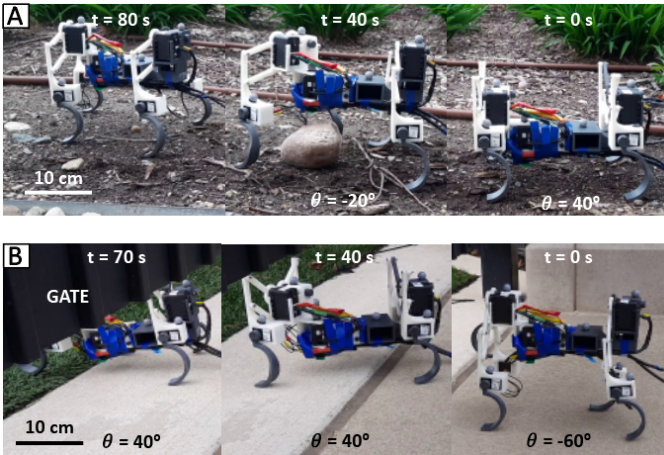


Fig. 9: Robot motion in outdoor environment (A) Overcoming a big rock on its path by changing posture from  $+40^\circ$  to  $-20^\circ$ , (B) Going inside the gate of a building by changing its posture from  $-60^\circ$  to  $+40^\circ$

without the use of any obstacle-detecting sensor. In Fig. 9 A, the robot can overcome a big rock on its path by changing its posture (SI movie- 4:43 to 5:00). Conversely, when the posture change is not applied, the robot becomes immobilized and remains stuck on the obstacle (SI movie- 5:01 to 5:12). Here, the robot changes its posture from  $+40^\circ$  to  $-20^\circ$ . In Figure 9 B, the robot demonstrates its ability to navigate through a building entrance by adopting a posture change from  $-60^\circ$  to  $+40^\circ$  (SI movie- 4:13 to 4:36). Without the posture change, the robot experiences a collision with the gate, resulting in a subsequent fall (SI movie- 4:37 to 4:42). These two experiments validate the importance of posture change in quadruped robots to adapt themselves to real-world environments. It may be noted that since the surfaces in outdoor settings are found to be very rough, the outdoor studies are conducted on legs without any rubber patches.

## V. CONCLUSION

This paper presents a quadruped robot inspired by crocodiles, designed to adjust its posture and body angle to adapt to unstructured environments. The robot utilizes a pair of symmetrical parallelogram mechanisms to adjust its posture in accordance with biological concepts, with each pair being actuated simultaneously by a single servo via a gear drive. This simple mechanism enables the robot to adjust both its height and width, thereby making it more adaptable. A bio-inspired approach is utilized to analyze the stability and gait selection of the robot. The CAD model of the robot is designed in Solidworks in a way that its center of gravity lies within the support polygon for most of the cycle. This design feature enables the robot to navigate unstructured environments without the need for posture-stabilizing sensors or learning algorithms. After the design, prototyping, stability analysis, and gait selection, the robot's posture-changing ability is tested in indoor and outdoor environments. The primary goals of the experiments are to avoid collisions, navigate through narrow channels, and overcome obstacles, and inclines. The robot achieves these tasks by employing posture

TABLE III: Suitable postures of the robot while moving in an unstructured environment

Environment Type	Posture Range (in degrees)	Summary
Narrow Tunnel Traversal	-60 to -40	The robot's width ( $d$ ) is minimum when it attains a posture between $-40$ and $-60$ degrees
Low Clearance Avoidance	20 to 40	The robot's height ( $H$ ) is minimum when it attains a posture between $+20$ and $+40$ degrees
Obstacle Avoidance	-60 to 0	The robot's ground clearance ( $h$ ) and width ( $d$ ) are greatest when it attains a posture of $-60$ and $0$ degrees, respectively
Ramp	0 to 40	The robot is mostly stable when it climbs with a posture between $0$ and $40$ degrees

changes and variable lateral undulation, which enable it to adapt to challenging terrains. One notable aspect of the work is that it aims to demonstrate the robot's robustness and adaptability without relying on learning algorithms or posture-maintaining sensors like Inertial Measurement Units (IMUs). Overall, the experiments emphasize the importance of the robot's ability to change its morphology (shape and posture) to overcome hurdles in terradynamically challenging environments, making it more adaptable and stable without the need for complex learning algorithms or sensing mechanisms. Moreover, the study identifies the direct impact of peak amplitude on stability during ramp experiments, emphasizing the proportional relationship between higher peak amplitudes and increased stability.

The current version of the robot showcases functionality, with its ability to navigate through various scenarios, including tunnels and obstacles, relying on pre-known distances derived from the robot's distance per cycle data. While this approach has proven effective, we acknowledge that integrating obstacle-detecting sensors could elevate the robot's capabilities and performance. With obstacle-detecting sensors, the robot can autonomously navigate its environment, avoiding obstacles in real-time. This is particularly important in dynamic environments where obstacles may appear unexpectedly. Also, while carrying out the experiments, several difficulties were faced with the wires. This is because the wires used to get entangled with legs leading to problems while carrying out experiments. Sometimes, the robot loses its stability due to unnecessary tension coming from the improperly entangled wires despite the careful design of the robot, regarding stability. Consequently, efforts for the robot's second version will prioritize an untethered robot design, aiming to enhance operational efficiency and overcome this occasional limitation. Ongoing research will also focus on integrating a bio-inspired, flexible tail to further enhance the robot's stability on slopes and irregular terrains. This comprehensive exploration establishes the presented robot as a promising example of adaptability and stability in terradynamically challenging environments.

## VI. ACKNOWLEDGMENT

We would like to express our appreciation to the members of Notre Dame MiNiRo-Lab for their invaluable contributions and insightful discussions.

### References

- [1] J. Bongard, "Morphological change in machines accelerates the evolution of robust behavior," *Proceedings of the National Academy of Sciences*, vol. 108, no. 4, pp. 1234–1239, 2011.
- [2] T. F. Nygaard, C. P. Martin, J. Torresen, K. Glette, and D. Howard, "Real-world embodied ai through a morphologically adaptive quadruped robot," *Nature Machine Intelligence*, vol. 3, no. 5, pp. 410–419, 2021.
- [3] M. Cianchetti, M. Calisti, L. Margheri, M. Kuba, and C. Laschi, "Bioinspired locomotion and grasping in water: the soft eight-arm octopus robot," *Bioinspiration & biomimetics*, vol. 10, no. 3, p. 035003, 2015.
- [4] S. Mintchev and D. Floreano, "Adaptive morphology: A design principle for multimodal and multifunctional robots," *IEEE Robotics & Automation Magazine*, vol. 23, no. 3, pp. 42–54, 2016.
- [5] C. D. Williams and A. A. Biewener, "Pigeons trade efficiency for stability in response to level of challenge during confined flight," *Proceedings of the National Academy of Sciences*, vol. 112, no. 11, pp. 3392–3396, 2015.
- [6] D. K. Riskin, A. Bergou, K. S. Breuer, and S. M. Swartz, "Upstroke wing flexion and the inertial cost of bat flight," *Proceedings of the Royal Society B: Biological Sciences*, vol. 279, no. 1740, pp. 2945–2950, 2012.
- [7] J. Brackenbury, "Caterpillar kinematics," *Nature*, vol. 390, no. 6659, pp. 453–453, 1997.
- [8] M. García-París and S. M. Deban, "A novel antipredator mechanism in salamanders: rolling escape in hydromantes platycephalus," *Journal of herpetology*, vol. 29, no. 1, pp. 149–151, 1995.
- [9] R. T. Bakker, "Dinosaur physiology and the origin of mammals," *Evolution*, pp. 636–658, 1971.
- [10] J. M. Parrish, "The origin of crocodylian locomotion," *Paleobiology*, vol. 13, no. 4, pp. 396–414, 1987.
- [11] S. M. Reilly and J. A. Elias, "Locomotion in alligator mississippiensis: kinematic effects of speed and posture and their relevance to the sprawling-to-erect paradigm," *Journal of Experimental Biology*, vol. 201, no. 18, pp. 2559–2574, 1998.
- [12] S. M. Reilly and J. A. Elias, "Locomotion in alligator mississippiensis: kinematic effects of speed and posture and their relevance to the sprawling-to-erect paradigm," *The Journal of experimental biology*, vol. 201, no. 18, pp. 2559–2574, 1998.
- [13] G.-n. Li, M. Zeng, Y. Ma, Q. Li, and W.-k. Xu, "Design of double-body car-snake hybrid transformable robot," in *2020 39th Chinese Control Conference (CCC)*, pp. 3881–3886, IEEE, 2020.
- [14] H. Jiang, G. Xu, W. Zeng, and F. Gao, "Design and kinematic modeling of a passively-actively transformable mobile robot," *Mechanism and Machine Theory*, vol. 142, p. 103591, 2019.
- [15] Z. Song, Z. Luo, G. Wei, and J. Shang, "A portable six-wheeled mobile robot with reconfigurable body and self-adaptable obstacle-climbing mechanisms," *Journal of Mechanisms and Robotics*, vol. 14, no. 5, p. 051010, 2022.
- [16] D. Zarrouk and L. Yehezkel, "Rising star: A highly reconfigurable sprawl tuned robot," *IEEE Robotics and automation letters*, vol. 3, no. 3, pp. 1888–1895, 2018.
- [17] O. Simhon, Z. Karni, S. Berman, and D. Zarrouk, "Overcoming obstacles with a reconfigurable robot using deep reinforcement learning based on a mechanical work-energy reward function," *IEEE Access*, vol. 11, pp. 47681–47689, 2023.
- [18] S. H. Derrouaoui, Y. Bouzid, and M. Guiatni, "Pso based optimal gain scheduling backstepping flight controller design for a transformable quadrotor," *Journal of Intelligent & Robotic Systems*, vol. 102, no. 3, p. 67, 2021.
- [19] B. W. Mulvey, T. D. Lalitharatne, and T. Nanayakkara, "Deformobot: A bio-inspired deformable mobile robot for navigation among obstacles," *IEEE Robotics and Automation Letters*, vol. 8, no. 6, pp. 3828–3835, 2023.
- [20] C. Zheng, S. Sane, K. Lee, V. Kalyanram, and K. Lee, "α-waltr: Adaptive wheel-and-leg transformable robot for versatile multiterrain locomotion," *IEEE Transactions on Robotics*, 2022.
- [21] S. Kim, S. Ryu, J. Won, H. S. Kim, and T. Seo, "2-dimensional dynamic analysis of inverted pendulum robot with transformable wheel for overcoming steps," *IEEE Robotics and Automation Letters*, vol. 7, no. 2, pp. 921–927, 2021.
- [22] Y. Ozkan-Aydin and D. I. Goldman, "Self-reconfigurable multilegged robot swarms collectively accomplish challenging teradynamic tasks," *Science Robotics*, vol. 6, no. 56, p. eabf1628, 2021.
- [23] J.-J. Chou and L.-S. Yang, "Innovative design of a claw-wheel transformable robot," in *2013 IEEE International Conference on Robotics and Automation*, pp. 1337–1342, IEEE, 2013.
- [24] X. Liang, M. Xu, L. Xu, P. Liu, X. Ren, Z. Kong, J. Yang, and S. Zhang, "The amphihex: A novel amphibious robot with transformable leg-flipper composite propulsion mechanism," in *2012 IEEE/RSJ International Conference on Intelligent Robots and Systems*, pp. 3667–3672, IEEE, 2012.
- [25] R. Baines, S. Freeman, F. Fish, and R. Kramer-Bottiglio, "Variable stiffness morphing limb for amphibious legged robots inspired by chelonian environmental adaptations," *Bioinspiration & Biomimetics*, vol. 15, no. 2, p. 025002, 2020.
- [26] D. Zambrano, M. Cianchetti, C. Laschi, H. Hauser, R. Fuchslin, and R. Pfeifer, "The morphological computation principles as a new paradigm for robotic design," *Opinions and outlooks on morphological computation*, pp. 214–225, 2014.
- [27] S. Kim, C. Laschi, and B. Trimmer, "Soft robotics: a bioinspired evolution in robotics," *Trends in biotechnology*, vol. 31, no. 5, pp. 287–294, 2013.
- [28] W. Wang, A. Ji, P. Manoonpong, H. Shen, J. Hu, Z. Dai, and Z. Yu, "Lateral undulation of the flexible spine of sprawling posture vertebrates," *Journal of Comparative Physiology A*, vol. 204, pp. 707–719, 2018.
- [29] B. Chong, Y. O. Aydin, C. Gong, G. Sartoretti, Y. Wu, J. M. Rieser, H. Xing, P. E. Schiebel, J. W. Rankin, K. B. Michel, et al., "Coordination of lateral body bending and leg movements for sprawled posture quadrupedal locomotion," *The International Journal of Robotics Research*, vol. 40, no. 4–5, pp. 747–763, 2021.
- [30] J. Qiu, A. Ji, K. Zhu, Q. Han, W. Wang, Q. Qi, and G. Chen, "A gecko-inspired robot with a flexible spine driven by shape memory alloy springs," *Soft Robotics*, 2023.
- [31] W. Haomachai, D. Shao, W. Wang, A. Ji, Z. Dai, and P. Manoonpong, "Lateral undulation of the bendable body of a gecko-inspired robot for energy-efficient inclined surface climbing," *IEEE Robotics and Automation Letters*, vol. 6, no. 4, pp. 7917–7924, 2021.
- [32] A. Spröwitz, A. Tuleu, M. Vespignani, M. Ajallooeian, E. Badri, and A. J. Ijspeert, "Towards dynamic trot gait locomotion: Design, control, and experiments with cheetah-cub, a compliant quadruped robot," *The International Journal of Robotics Research*, vol. 32, no. 8, pp. 932–950, 2013.
- [33] M. Kalakrishnan, J. Buchli, P. Pastor, M. Mistry, and S. Schaal, "Learning, planning, and control for quadruped locomotion over challenging terrain," *The International Journal of Robotics Research*, vol. 30, no. 2, pp. 236–258, 2011.
- [34] S. Seok, A. Wang, M. Y. Chuah, D. J. Hyun, J. Lee, D. M. Otten, J. H. Lang, and S. Kim, "Design principles for energy-efficient legged locomotion and implementation on the mit cheetah robot," *Ieee/asme transactions on mechatronics*, vol. 20, no. 3, pp. 1117–1129, 2014.
- [35] U. Saranlı, M. Buehler, and D. E. Koditschek, "Rhex: A simple and highly mobile hexapod robot," *The International Journal of Robotics Research*, vol. 20, no. 7, pp. 616–631, 2001.
- [36] M. Gor, P. M. Pathak, A. Samantaray, K. Alam, P. Kumar, D. Anand, P. Vijay, R. Sarkar, J. Yang, and S. Kwak, "Development of a compliant legged quadruped robot," *Sādhanā*, vol. 43, pp. 1–18, 2018.
- [37] Y. Ansari, A. L. Shoushtari, V. Cacucciolo, M. Cianchetti, and C. Laschi, "Dynamic walking with a soft limb robot," in *Biomimetic and Biohybrid Systems: 4th International Conference, Living Machines 2015, Barcelona, Spain, July 28–31, 2015, Proceedings 4*, pp. 13–25, Springer, 2015.
- [38] I. Juárez-Campos, D. A. Núñez-Altamirano, L. Márquez-Pérez, L. Romero-Muñoz, M. E. Juárez-Campos, and B. Juárez-Campos, "Bioinspired sprawling robotic leg and a path-planning

- procedure,” *International Journal of Advanced Robotic Systems*, vol. 15, no. 1, p. 1729881418759888, 2018.
- [39] D. Li, Z. Zhang, J. S. Dai, and J. M. McCarthy, “Configuration synthesis of metamorphic mechanisms based on characteristic incidence matrix,” in *International Design Engineering Technical Conferences and Computers and Information in Engineering Conference*, vol. 44106, pp. 943–952, 2010.
- [40] J. J. Uicker, G. R. Pennock, J. E. Shigley, and J. M. McCarthy, *Theory of machines and mechanisms*, vol. 768. Oxford University Press New York, 2003.
- [41] N. Neville and M. Buehler, “Towards bipedal running of a six legged robot,” in *12th Yale Workshop on Adaptive and Learning Systems*, vol. 12, pp. 1–7, 2003.
- [42] E. Moore, D. Campbell, F. Grimmering, and M. Buehler, “Reliable stair climbing in the simple hexapod ‘rhex,’” in *Proceedings 2002 IEEE International Conference on Robotics and Automation (Cat. No.02CH37292)*, vol. 3, pp. 2222–2227 vol.3, 2002.
- [43] R. Altendorfer, N. Moore, H. Komsuoglu, M. Buehler, H. Brown, D. McMordie, U. Saranli, R. Full, and D. E. Koditschek, “Rhex: A biologically inspired hexapod runner,” *Autonomous Robots*, vol. 11, pp. 207–213, 2001.
- [44] A. Vina and A. Barrientos, “C-legged hexapod robot design guidelines based on energy analysis,” *Applied Sciences*, vol. 11, no. 6, p. 2513, 2021.
- [45] Y. O. Aydin, A. Saranli, Y. Yazicioglu, U. Saranli, and K. Leblebicioğlu, “Optimal control of a half-circular compliant legged monopod,” *Control Engineering Practice*, vol. 33, pp. 10–21, 2014.
- [46] E. Moore, “Leg design and stair climbing control for the rhex robotic hexapod. department of mechanical engineering mcgill university,” 2002.
- [47] Y. O. Aydin, K. C. Galloway, Y. Yazicioglu, and D. E. Koditschek, “Modeling the compliance of a variable stiffness c-shaped leg using castigliano’s theorem,” in *International Design Engineering Technical Conferences and Computers and Information in Engineering Conference*, vol. 44106, pp. 705–713, 2010.
- [48] “Robotis dynamixel sdk.” [https://emanual.robotis.com/docs/en/software/dynamixel/dynamixel\\_sdk/library\\_setup/matlab\\_windows/](https://emanual.robotis.com/docs/en/software/dynamixel/dynamixel_sdk/library_setup/matlab_windows/). Accessed: 2022-12-15.
- [49] “Dynamixel control modes.” <https://www.dynamixel.com/whatisdxl.php>. Accessed: 2022-12-15.
- [50] R. B. McGhee and A. A. Frank, “On the stability properties of quadruped creeping gaits,” *Mathematical Biosciences*, vol. 3, pp. 331–351, 1968.
- [51] M. Hildebrand, “Symmetrical gaits of horses: Gaits can be expressed numerically and analyzed graphically to reveal their nature and relationships,” *Science*, vol. 150, no. 3697, pp. 701–708, 1965.
- [52] R. Tomovic, “A general theoretical model of creeping displacement,” *Cybernetica*, vol. 4, no. 2, 1961.
- [53] J. Gray, “Studies in the mechanics of the tetrapod skeleton,” *Journal of Experimental Biology*, vol. 20, no. 2, pp. 88–116, 1944.
- [54] M. Hildebrand, “The adaptive significance of tetrapod gait selection,” *American Zoologist*, vol. 20, no. 1, pp. 255–267, 1980.
- [55] M. Hildebrand, “The quadrupedal gaits of vertebrates,” *Bioscience*, vol. 39, no. 11, p. 766, 1989.
- [56] R. B. McGhee, “Some finite state aspects of legged locomotion,” *Mathematical Biosciences*, vol. 2, no. 1-2, pp. 67–84, 1968.